Tesseract - A High-Stability, Low-Noise Fluxgate Sensor Designed for Constellation Applications

Kenton Greene[1], Christian Hansen[1], B. Barry Narod[2], Richard Dvorsky[1], David M. Miles[1]

[1]Department of Physics and Astronomy, University of Iowa, Iowa City, IA, USA

5   [2]Department of Earth, Ocean and Atmospheric Sciences, University of British Columbia, Vancouver, Canada

Correspondence to: Kenton Greene (kenton-greene@uiowa.edu)

Abstract. Accurate high-precision magnetic field measurements are a significant challenge for many applications including constellation missions studying space plasmas. Instrument stability and orthogonality are essential to enable meaningful comparison between disparate satellites in a constellation without extensive cross-calibration efforts. Here we describe the design

10   and characterization of Tesseract - a fluxgate magnetometer sensor designed for low-noise, high-stability constellation applications. Tesseract's design takes advantage of recent developments in the manufacturing of custom low noise fluxgate cores. Six of these custom racetrack fluxgate cores are securely and compactly mounted within a single solid three-axis symmetric base. Tesseract's feedback windings are configured as a four-square Merritt coil to create a large homogenous magnetic null inside the sensor where the fluxgate cores are held in near-zero field, regardless of the ambient magnetic field, to improve the reliability of the core

15   magnetization cycle. A Biot-Savart simulation is used to optimize the homogeneity of field generated by the feedback Merritt Coils and was verified experimentally to be homogeneous within 0.42 percent along the racetrack cores' axes; an improvement thirteen times that of the traditional ring-core sensor design. The thermal stability of the feedback windings is measured using an insulated container filled with dry ice inside a coil system. The sensitivity over temperature of the feedback windings is found to be between 13 ppm/°C and 17 ppm/°C. The sensor's three axes maintain orthogonality to within at most 0.015 degrees over a temperature

20   range of -45 °C to 20 °C; an improvement at least six times that of the ring-core sensor design. Tesseract's cores achieve a magnetic noise floor of 5 pT/√Hz at one Hz. Tesseract will be flight demonstrated on the ACES-II sounding rockets, currently scheduled to launch in late 2022 and again aboard the TRACERS satellite mission as part of the MAGIC technology demonstration which is currently scheduled to launch in 2023.

1 Introduction

25   Constellation satellite missions are acknowledged to have an important role in the future of space plasma science. The NASA Heliophysics Science and Technology Roadmap for 2014–2033, recognizes that one of the opportunities to drive scientific discovery will come from a constellation mission of 30 or more spacecraft (Heliophysics Roadmap 2014). Recent missions such as Cluster (Balogh et al., 2001), Swarm (Merayo et al., 2008), ST-5 (Slavin et al., 2008), THEMIS (Auster et al., 2008) and The

30   Magnetospheric Multiscale Mission (Torbert et al., 2016) have successfully flown constellations of three to five spacecraft and have made significant contributions to the understanding of solar wind and magnetospheric physics (Ganushkina et al., 2017., Nakariakov et al., 2016 and the references therein).

Recent developments in nanosatellite technology promise to provide a platform for the future of constellation missions at a low cost (Bandyopadhyay et al., 2015). Such a nanosatellite constellation mission could accurately resolve and characterize the spatial

35   and temporal evolution of magnetic fluctuations that are indicative of larger scale magnetospheric processes, such as plasma waves,

field aligned currents and plasma transport at various scales. However, constructing a magnetic sensor with sufficiently small mass and volume to be accommodated on a nanosatellite, while still maintaining the instrumental accuracy and precision required for a magnetospheric constellation mission is not a trivial task. As the size of a fluxgate sensor is reduced, it becomes increasingly difficult to preserve the stability required for reliable multi-point cross-comparisons. This presents a significant challenge for the

40 use of nanosatellites on constellation missions. The 2015 NASA Technology Roadmap has noted the importance of addressing the challenge of "high measurement stability to allow inter-satellite calibration" to enable "high-stability magnetic field measurements that can be made in distributed systems" (2015 NASA Technology Roadmap 8.3.1.3).

1.1 Fluxgate Stability

Fluxgate stability is critically important for a magnetospheric constellation mission, as it enables comparison of disparate magnetic

45 measurements without the need for intensive cross calibration. However, it remains poorly understood and is not explicitly addressed by many authors in the literature. Factors suspected of degrading fluxgate stability include an inhomogeneous magnetic null (Ripka, 1992) and skewing of the axes and cores due to mechanical and thermal strain (Primdahl, 1979).

Fluxgate magnetometers (Primdahl, 1979) measure the static and low-frequency vector magnetic field by modulating or gating the local magnetic flux and measuring the induced electromagnetic force (EMF) in a sense winding. A ferromagnetic core, periodically

50 driven into magnetic saturation at frequency f, is used to gate the local field, thereby inducing a second harmonic ($2f$) signal due to the nonlinear magnetic permeability of the core as it enters magnetic saturation twice per cycle. In this paper, we will be discussing only second harmonic fluxgates. In many instruments, including that presented here, magnetic feedback is used to null the magnetic field in the sensor, which linearizes and extends the measurement range of the instrument and is thought to improve overall fluxgate stability (Primdahl and Jensen, 1982). Magnetic sensors that are nulled in two axes, such as the CASSIOPE/e-

55 POP fluxgate which maintained a sensitivity stability of approximately of 18 ppm/°C (Wallis et al., 2015), outperform sensors zeroed in only a single component i.e. Narod and Bennest, (1990); Acuña et al (1978), which achieved a stability of ± 0.25% (Acuña et al., 1978) over the temperatures ranges from -20°C to 40°C which we calculate is equivalent to 26 ppm/°C. Thus, we hypothesize that a null in all three axes will further improve stability compared to one or two axis nulled sensor designs.

1.2 Current State of High Stability Fluxgate Sensors

60 Recent constellation missions have increasingly focused on flying three axis compensated sensors in the interest of maximizing instrumental stability. However, sensor designs that have flown on past constellation missions have been constrained to accommodate a traditional one-inch diameter ring-core geometry ferromagnetic core.

Potentially the most stable magnetospheric field fluxgate measurements to date were taken with the Compact Spherical Coil (CSC) Sensor aboard Swarm which implements a nested three axis Helmholtz coil feedback wound on a MACOR shell to create a three-

65 axis null in a 100×100×50 mm instrument. The 500g CSC sensor has maintained a sensitivity stability over temperature of 10 ppm/°C and very high axis stability of 0.002 degrees from -20°C to 40°C while achieving a noise floor of 6.6 pT/√Hz at 1 Hz (Merayo et al., 2008). From Primdahl and Jenson (1982), we estimate that the CSC's feedback coils hold their ring-cores in a field that deviates from uniformity by 1.5%.

The THEMIS mission incorporated 70×70×45 mm fluxgate sensors that achieved a sensitivity stability of 22 ppm/°C, an axes'

70 stability within 0.017 degrees and a noise of 10 pT/Hz at 1 Hz (Auster et al., 2008). The ST-5 magnetometer (MAG) has dimensions of 50×50×30 mm and a total mass with electronics of approximately 600g and achieved a noise of 0.1 nT rms at 1 Hz. (Slavin et

al., 2008). The Magnetospheric Multiscale Mission 42.4×44.3×48.7 mm DFG instrument achieved a noise floor of 8pT/√Hz at 1 Hz, an axis stability of about 0.03 degrees between -50°C and 30°C, and a sensitivity stability over temperature of 30 ppm/°C after compensation was applied (Russell et al., 2016). Notably, the temperature dependent sensitivity can be corrected to first order by

75 fluxgate electronics using compensated feedback current (Primdahl 1970; Acuña et al., 1978; Miles et al., 2017); however, no equivalent compensation exists for orthogonality. In general, smaller temperature dependent sensitivity is desirable but smaller orthogonality dependence is more critical.

Future constellation missions, such as Geospace Dynamics Constellation (Pfaff et al., 2016), MagneToRE (Maruca et al., 2021) and NanoSWARM (Gerrick-Bethell et al., 2021) promise to build on the success of these constellation magnetometers, and the

80 continued development of increasingly precise, robust, magnetic field instruments remains an important means to these efforts.

1.3 Current State of Miniaturized Fluxgate Sensors

Nanosatellites as a platform for magnetospheric measurements are an emerging topic in the literature. Some tend to focus on miniaturizing traditional fluxgate magnetometer designs for CubeSat applications without overly compromising their measurement capability (e.g., Ripka, 2003 and references therein). Recent missions, such as Dellingr and ExAlta1, have implemented

85 miniaturized, boom-deployed fluxgate magnetometers on nanosatellites. The Dellingr nanosatellite flew a very small 19g fluxgate magnetometer with a noise floor of 120 pT/√Hz at 1 Hz (Kepko et al., 2017). The Ex-Alta 1 CubeSat flew a 47g miniaturized fluxgate sensor with a noise floor of 150pT/√Hz at 1 Hz (Miles et al., 2016). However, these miniature instruments typically sacrifice noise and stability in the interest of small size. With a stability poorer than 50 ppm/°C, these sensors function primarily as variometers. If used in a constellation setting, measurements from disparate sensors would be far less comparable than those

90 from previous constellation mission without complex and time-consuming cross calibration. One of the best small sensors to date appears to be the Small Magnetometer in Low-mass Experiment (SMILE) developed by Forslund et al (2007), which achieved a thermal sensitivity stability of 11 ppm/°C, an axis stability better than 0.02 degrees from -30 to 45°C, and 30pT/√Hz at 1Hz with a 40g, 20×20×20 mm cubic sensor based on three rod cores within a three-axis feedback winding (Forslund et al., 2007).

1.4 Tesseract Sensor Overview

95 Like the CSC and SMILE sensors, Tesseract's feedback windings create a three-axis 'magnetic null' inside the sensor where the fluxgate cores are held in near-zero field. This ensures that the cores do not exceed their linear sensitivity region regardless of the magnitude of the ambient magnetic field (Primdahl and Jensen, 1982). An inhomogeneous magnetic null at the cores is known to be a primary contributor to degrading fluxgate stability (Ripka, 1992).
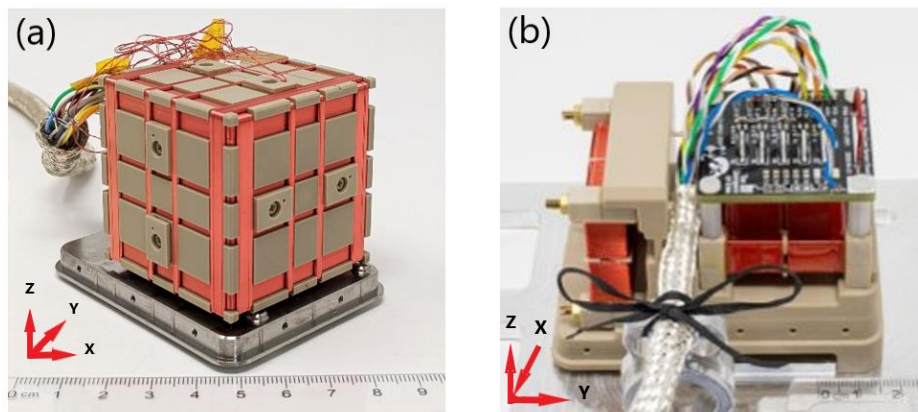
Figure 1: (a) A high fidelity prototype of the Tesseract sensor has been constructed for testing in preparation for MAGIC: a technology demonstration on the TRACERS satellite mission Tesseract's feedback coils are arranged in a three axis four-loop Merritt coil which is expected to create a large homogenous null region in the sensor. Tesseract's feedback coils are wound on a common base of 30% glass filled Torlon. (b) The traditional one-inch diameter ring-core sensor used in the testing described in this paper.

Here, we present the design and characterization of Tesseract: a high-stability fluxgate magnetometer for constellation missions. The Tesseract sensor's three-axis feedback windings are arranged in a four-square Merritt coil, which creates a proportionally larger homogeneous region than the Helmholtz coil for the same external volume (Merritt, 1983) allowing it to accommodate more cores (six instead of three). Tesseract's Merritt coil feedback winding has been optimized to hold these cores within a highly homogeneous null field (deviations from average of less than 0.42%), which allows for a reproducible magnetization of the ferromagnetic cores. This reproducibility is designed to improve the measurement stability of the sensor.

Parameters	Tesseract Sensor	Ring-core Sensor
Sensor Dimensions	50 x 50 x 50 mm	22 x 28 x 30 mm
Sensor Mass	340g	287g
Feedback Power Consumption at 65000 nT Earth Field	29.7 mW	14.4 mW
Noise Floor of Cores	5 pT/√Hz at 1 Hz	7 pT/√Hz at 1 Hz
Uncompensated Stability over Temperature*	13 - 17 ppm/°C	11 - 26 ppm/°C
Axis Orthogonality Angles Stability over Temperature*	< 0.015 Degrees	0.09 Degrees
Feedback Field Homogeneity at Cores	< 0.42%	< 5.62%

* In the range from -45 °C to 20 °C

Table 1: The Tesseract Sensor's specifications as measured in the laboratory compared with the specifications of a more traditional ring-core sensor design. Tesseract is marginally larger than the ring-core sensor but has much higher axis stability and magnetic feedback homogeneity, which are associated with higher instrumental stability. The Uncompensated Stability and Orthogonality angles are both measured from -45°C to 20°C

Tesseract's custom low noise racetrack geometry cores are securely and compactly mounted within a single solid three-axis symmetric base of 30% glass-filled Torlon, reducing the potential for mechanical strains due to uneven coefficients of linear expansion and reducing the tendency of the sensor to skew with temperature, thus limiting these potential sources of instrument instability. Tesseract's cores achieve a magnetic noise floor of 5 pT/√Hz at one Hz, an orthogonality within 0.015 degrees and temperature stability of 13-17 ppm/°C between -45°C and 20°C.

2 Sensor Design

Tesseract is designed to mitigate known sources of instability such as uncompensated residual field inside the sensor and skewing
125   of the axes and the cores due to mechanical and thermal stresses while still maintaining low noise and a small size. Here we
describe the design, optimization, manufacturing, and assembly processes for the Tesseract sensor.

2.1 Racetrack Core Design

The noise floor of a fluxgate is typically limited by the intrinsic magnetic noise of a permalloy core that is periodically driven into
magnetic saturation to modulate the local magnetic field. Recent development in custom low noise core manufacturing by Miles
130   (2019) enabled us to create custom low-noise miniature racetrack sensors (Miles et al., 2022).

Custom permalloy created using the Miles et al., 2022 process is cold rolled into 50 µm thick foil. The permalloy foil is then cut
to 5 cm length, stacked, drilled, and secured in a tight bundle. A milling machine was used to machine 6.45 mm wide by 31.45
mm long racetrack foil washers. The racetrack washers are placed in the furnace, heat-treated, and stacked into a Torlon bobbin
(Figure 2a) and interleaved with insulating layers of Kapton of the same geometry.
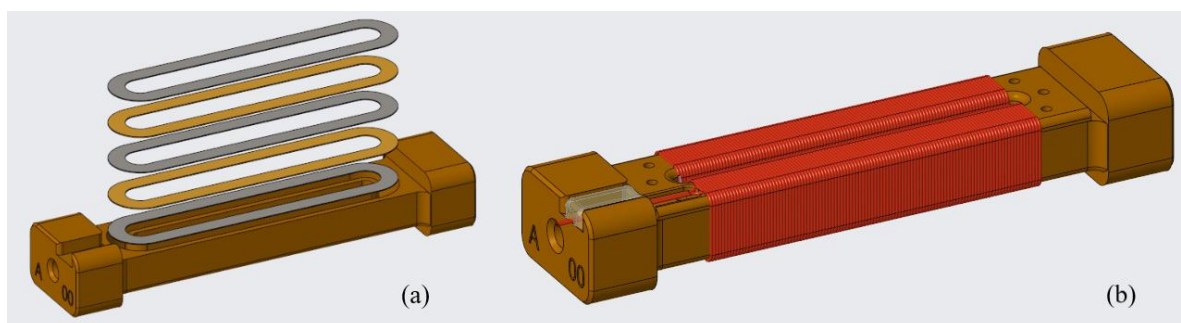
135   **Figure 2: (a) Layers of foil loops are stacked within a Torlon bobbin with layer of Kapton placed in between permalloy layers. (b) The
bobbin serves as a frame for the drive coils which are wound on the two long racetrack supports.**

A plastic lid closes the core and serves as a base upon which to wind a quasi-toroidal drive of AWG 32 magnet wire (Figure 2b).
Production cores are interleaved with a polymer between the foil layers to prevent them from moving during the magnetizing drive
140   pulses. The stacked foil washers remove the need to spot-weld, as is done in traditional spiral-wound sensors, avoiding the heat-
affected area around the weld and its unpredictable magnetic properties. Heat-treating the foil washers individually removes the
risk of undesired welding between layers that can cause unintended shorting.

The race-track geometry aligns ferromagnetic mass on one axis, producing lower noise. However, the race-track geometry cannot
be double-wound like a ring-core to sample two orthogonal components. The closed flux path of the racetrack should reduce stray
145   fields and offset error compared to traditional parallel rod sensors (e.g., Janosek 2017; Moldovanu et al., 2000).

2.2 Sensor Base Design

Tesseract leverages this racetrack geometry to create a compact sensor. Six of these custom racetrack geometry cores are fixed
within a three-axis symmetric 30% glass filled Polyamide-Imide (Torlon 5030) base in a compact configuration of two cores per
axis shown in Figure 3a. This pairing of identical cores with opposite polarities in each axis is expected to further reduce the
150   tendency for cross-axis contamination due to stray fields.

These cores are then secured firmly in place using polymerics and nonmagnetic screws so that they do not shift during vibration,
but without exerting any mechanical stress on the core (Figure 3b). Vacuum tolerant epoxy is used to secure the drive windings to

the cylindrical walls of the bobbin, thereby locking the drive winding in place without creating a rigid bond to the racetrack core. The foil bobbin and the sensor base are manufactured from the same glass filled Torlon which will reduce the impact of mismatched

155 coefficients of linear thermal expansions compared to sensors using the traditional Inconel bobbin. This further reduces the potential for mechanical stress.
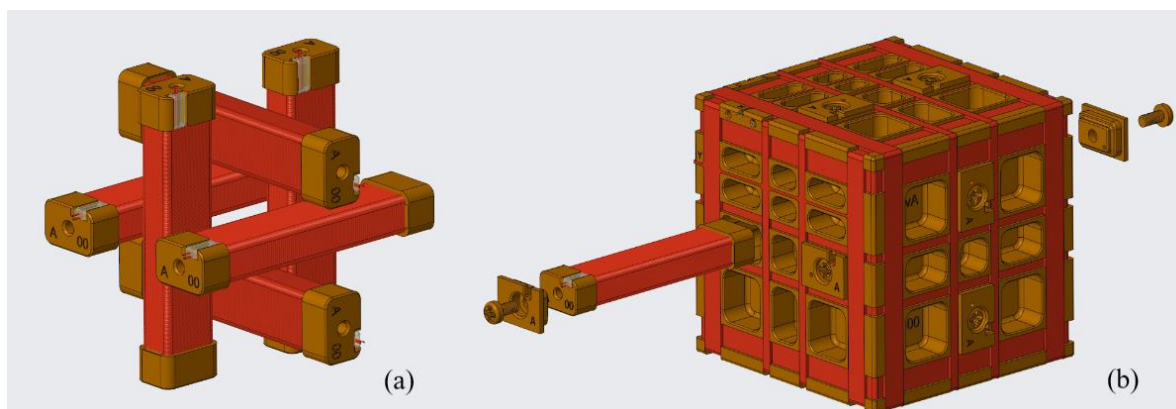
Figure 3: (a) Tesseract's six miniature racetrack cores are wound with a sense winding, arranged in pairs/two per axis and (b) secured within one common Torlon base. The Tesseract sensor's Merritt coil feedback windings are wound in small, machined channels in this
160 **base.**

Torlon is lighter and much easier to machine than the traditional Inconel ringcore bobbin or MACOR sensor winding. Small channels of a predetermined width and depth are precisely and symmetrically machined into a Torlon block. This block serves as a common base upon which to wind Tesseract's three orthogonal feedback coils (3b in red) This single solid 3 axis symmetric base

165 for all three sense coil axes is expected to further reduce the tendency of the sensor's axes to skew with temperature, thus preserving the orthogonality.

Additionally, a common base for the feedback windings provides a small, linear temperature dependence that can be characterized and then compensated in electronics. Fluxgate sensor measurements have long been known to vary with temperature (e.g., Trigg et a1., 1971). Miles (2017) documents the historical technique (Acuña, 1978) of providing realtime analog temperature

170 compensation. Temperature compensation can be provided electronically in real time by modifying the feedback current. A transconductance amplifier can be modified such that the normally constant voltage-to-current transfer function is engineered to respond to the load resistance provided by RTDs which are mounted in series with the feedback. This scaling of this transfer function allows, to first order, the effect of temperature on the load resistance offered by the sense winding to compensate for the effect of temperature on the sensor geometry.

175 The compensation is limited to the linear scaling of this transfer function, so it requires that the sensor be highly mechanically stable with temperature such that its thermal sensitivity dependence is functionally linear through the operating temperature range. 30% glass filled Torlon has a very linear response to temperature and with a thermal expansion coefficient of 16.2 ppm/°C, making it an excellent base material for linear sensitivity temperature compensation. There are materials with a lower coefficient of thermal expansion, Torlon was selected to match the thermal expansion coefficient of the copper windings (16.7 ppm/°C) and minimize

180 stress in the sensor. Tesseract takes advantage of this property of Torlon for effective real time linear temperature compensation, which should contribute to good measurement stability over changes in temperature. Torlon is also extremely resistant to shearing and skewing with temperature. We expect that this will reduce the tendency of the sensor's axes to skew with temperature.

2.3 Feedback Winding Design

Tesseract's three orthogonal feedback coils are wound into channels that have been machined symmetrically into the Torlon base
185 (Figure 3b). A CNC winding machine is used to guide 40 AWG magnet wire into the channels so that there is no asymmetry or
overlap. These feedback windings create a three-axis 'magnetic null' inside the sensor where the racetrack fluxgate cores are held
in near-zero field. This ensures that the cores do not become oversaturated and exceed their linear sensitivity region regardless of
the magnitude of the ambient magnetic field (Primdahl and Jensen, 1982). Retaining the cores in a homogeneous region, where
the magnetic field can be effectively nulled, helps to ensure a reproduceable magnetization of the ferromagnetic cores. This is
190 thought to improve the sensor's measurement stability and linearity (Ripka, 1992). Tesseract's feedback windings are arranged as
a four-square Merritt Coil in three axes. This configuration creates a relatively large homogeneous region relative to the coil's
volume compared to a traditional Helmholtz Coil (Merritt, 1983)

2.3.1 Feedback Field Simulation

To analyze and optimize the design of the Tesseract sensor's feedback windings, we developed a Biot-Savart simulation of the
195 magnetic field generated by these windings when a DC current is applied. The simulation of the magnetic field generated by the
Tesseract's x-axis feedback coils, rendered in Figure 4a, is as a slice at the plane z=0 (Figure 4b). The main region of interest is
the area occupied by racetrack cores (outlined in maroon), which is at z =0 mm, y = ± 12 mm, and x = ± 15 mm. For the purposes
of this paper, the figure of merit for a feedback winding configuration will be the degree to which this winding holds the racetrack
core axis in a homogeneous field; more explicitly, the maximum percentage that the magnetic field values along the y = 12 mm
200 axis deviates from the average field along this axis.
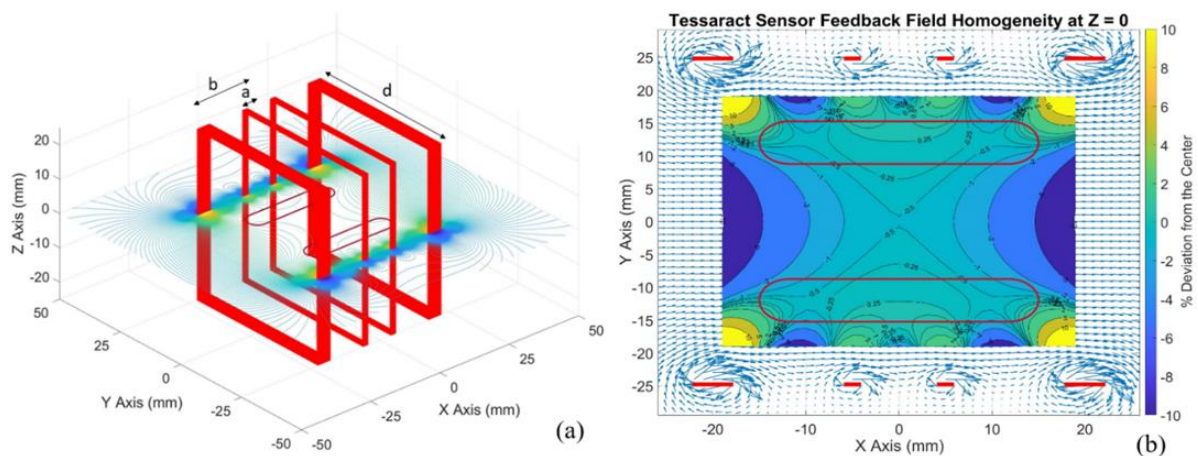
**Figure 4: (a) A four square Merritt coil system is the basis of the design for the Tesseract sensor's feedback windings. A Biot-Savart
simulation of the Tesseract's feedback winding models each loop of wire as a square array are assigned a position on a 3D grid. (b) A
two-dimensional cross section at z = 0 of the Biot-Savart model of the Tesseract sensor. The maroon loops outline the regions where the
205 racetrack sensors are situated. The contours plot the percentage of deviation of the field from its average along the axis of the racetrack
cores (y = +12 mm, -12 mm). In this region, maximum deviation of the magnetic field from the average field along the racetrack core is
about 0.42%. Blue arrows map out the direction and magnitude of the B field, while the red dots represent the positions of the wires.**

The simulation of the Tesseract sensor's feedback design suggests that the deviation from a uniform magnetic field along the 1D
210 axis of the racetrack core (at y =+12 mm) does not exceed 0.45% (Figure 4b). We surmise that keeping Tesseract's racetrack cores
immersed in this highly magnetically homogeneous region will contribute more stable, linear fluxgate performance.

In this simulation, each loop of wire in the Merritt Coil is modeled as a square array with an assigned length, current and a location on a 3D grid (Figure 4a). A Biot-Savart integration is applied over each element in the square array to evaluate the magnetic field at every point on this grid. This process is repeated for every loop in the coil system, and the resulting field values are summed to
215 create a model of the total magnetic field generated by a Merritt coil system.

2.3.2 Feedback Winding Optimization

Merritt (1983) provides a natural starting place for constraining the possible positions of the wires. The classic four-square Merritt coil design, rendered in Figure 4a, groups wires into four 'channels', two outer channels and two inner channels, and places constraints on the size and position of each channel. The distance of the outer channel b and inner channel a from the center (labeled
220 at the top of Figure 4a) must be related to the length of the coil d, such that a/d = 0.1281 and b/d = 0.5055. Additionally, the ideal Merritt coil geometry places constraints on the number of wire turns in each channel. For example, the number of wire turns on the inner channel must be 0.4235 times the number of turns on the outer channel (Merritt et al., 1983).

However, given the physical constraints of manufacturing a three-axis sensor, it is necessary to violate these ratios slightly. The requirement for channel spacing must be broken such that b/d < 0.5 in order to maintain three-axis symmetry and the mechanical
225 integrity of the Torlon. Other considerations about the winding (i.e. that the number of layers must be even to ensure that the terminating leads start and end in the same place so they can be terminated in a twisted pair) places further restrictions in the model. When all these constraints are applied, we are left with the wire gauge, number of wire turns, and the ratio of the number of inner loops to outer loops as parameters that can vary. The Biot-Savart model (Figure 4b) was used to simulate 72 possible feedback winding configurations and the results were analyzed to determine which feedback winding characteristics were optimal for
230 generating a homogenous field along the axis of the racetrack cores.
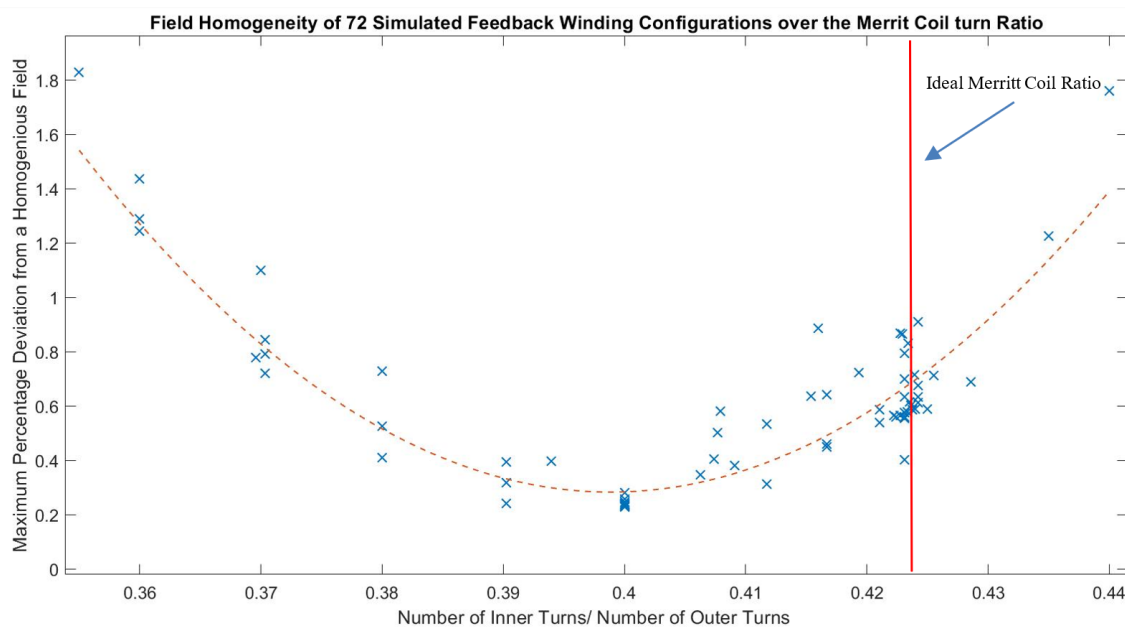
Figure 5: The percentage that the field along the racetrack core axis (at y = 12 mm, between x = 15 mm and -15 mm) deviates from average plotted against the ratio of inner loops of wire to outer loops. Seventy-two feedback winding configurations were simulated using the Biot-Savart model. The results of the simulation showed a relationship between the ratio of inner turns to outer
235 **turns with the homogeneity of the magnetic field. A quadratic fit with an R squared value of 0.8 suggests that an inner to outer turn ratio of 0.3985 is optimal for homogeneity.**

The field homogeneity generated by a feedback winding was found to have a dependence on that winding's ratio of inner loops to outer loops. Figure 5 plots the percentage that the field at the racetrack core deviates from uniformity against the ratio of inner loops of wire to outer loops. A quadratic fit suggests that an inner to outer loop ratio of 0.3985 is optimal for homogeneity. This differs from the classic Merritt coil ratio of 0.4236. Shifting the inner to outer loop ratio compensates the earlier violation of the channel distance requirements for b/d defined in section 2.3.1 that were necessary to construct a physical sensor. Other parameters (wire gauge and total number of wire loops of the feedback winding) were not found to have a discernable correlation with the homogeneity of the feedback magnetic field.

In addition to feedback field homogeneity, another important consideration in selecting an optimal feedback configuration for a magnetospheric sensor is the power dissipation required for these feedback windings to null maximum earth field ~65000 nT. This power consumption per axis was calculated using the equation from Magdaleno-Adame, (2010):

$$P_{max} = I_{max} \, V = \frac{B_{max} \, d}{1.795 x 10^{-6} * N} \, V \tag{1}$$

Where N is the total number of turns of wire, d is the length of one side of the square coil (as demarcated in figure 4), and for our purposes: V = 5 volts (the maximum voltage allowed by the operational amplifier) and B = 65000 nT (the maximum field experienced in orbit). This equation implies an inverse relationship between feedback power consumption at earth field P_{max} and the total number of loops of wire N. Thus, a feedback configuration with more loops of wire will require less power to null earth field with an upper limit of on the resistance of the coil of $\frac{V}{I_{max}}$ to ensure it can null the full field.

Of these 72 simulated feedback winding configurations, three were determined to be excellent candidates for good feedback homogeneity and power efficiency. Figure 6 shows the parameters of these configurations along with the modeled magnetic flux density distribution along the axis of the racetrack core for each of these optimized feedback configurations.
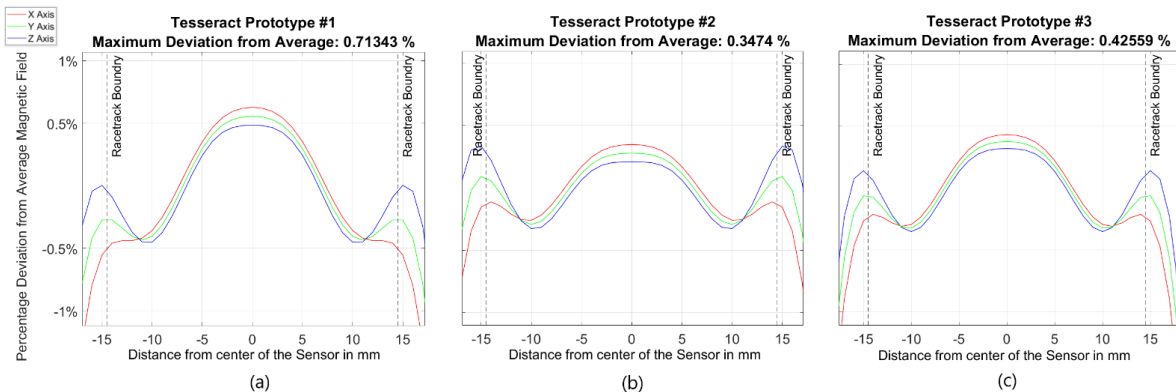
Figure 6: Homogeneity of the feedback magnetic field along the axis of the racetrack core for each axis of three optimized sensors. The racetrack core occupies the region between the vertical dashed black lines at –15mm and 15mm. Configuration (b) was optimized for best homogeneity while sensor while (c) was chosen for good homogeneity with very low power consumption.

The configuration in Figure 6c with 864 turns and a wire gauge of 40 AWG was determined to be a suitable balance of good homogeneity and feedback power efficiency. The magnetic field along the racetrack core axis varies by less than 0.46% in the x axis, 0.38% in the y axis and 0.32% on the z axis. This design requires a sensor power consumption of 89.1 mW to compensate for a worst-case Earth field of 65000 nT, which is very reasonable for accommodation on a small satellite. This is the feedback winding design that we plan to implement on the flight-ready Tesseract magnetometer that will be flown on the ACES-II sounding rockets and again on the TRACERS satellites mission.

3 Sensor Characterization

270   The Tesseract sensor design was prototyped and subjected to a series of tests in order to evaluate the validity of our design models and to quantitatively characterize the sensor's performance. First, several prototype sensors were manufactured and tested for feedback winding homogeneity and stability over temperature. From the results of these initial tests, as described in this section, we selected the prototype that exhibited the most homogeneous feedback field.

Then, a high-fidelity prototype was manufactured with the specifications shown in Table 1. A series of tests were conducted on this prototype to quantify the characteristics of the Tesseract sensor: the feedback field uniformity , the sensitivity and orthogonality

275   over changes in temperature, and the noise floor of the core. All the tests described in this section were conducted at the University of Iowa Magnetometer Calibration Facility.

3.1 Feedback Field Homogeneity

In order to experimentally characterize the magnetic field generated by the feedback windings and test the results of the Biot-Savart model, three prototype sensors were manufactured with the optimized feedback winding configurations modeled in Figure

280   6. For our purposes, we are most interested quantifying the homogeneity of the feedback magnetic field along the axis of the racetrack core. Each prototype sensor was placed within a single axis solenoid within a three-layer mumetal magnetic shield and constant current of 20 mA was applied to the feedback windings. A DC hall effect milligauss meter probe was placed in the center of the racetrack core's rectangular bore hole in the prototype bobbin and measurements of the magnetic field generated by this current were taken along the bore axis at 2.5 mm intervals. The final value for each measurement was found as an average of that

285   value over four separate tests. The uncertainty was determined by the range over which each measured magnetic field value varied over the four tests. Figure 7 plots the measured magnetic flux distribution along the longest axis of the racetrack core for each prototype sensor as a percentage deviation from the average field value along the bore hole axis between -15mm and 15mm (the domain of the racetrack core).
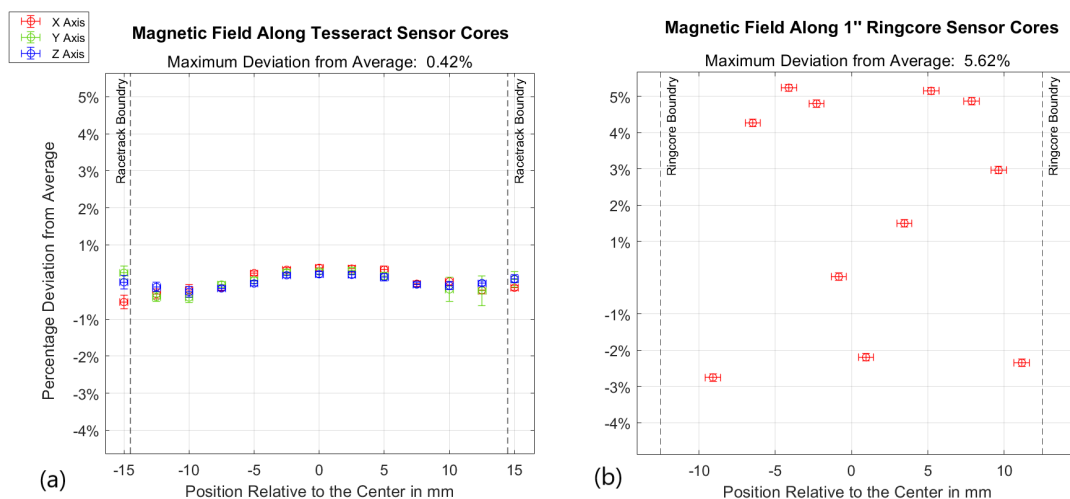
290

Figure 7: (a) The magnetic field generated by the Tesseract prototype #3 sensors' feedback windings was measured in 2.5 mm intervals along the axis of the racetrack bore hole. The magnetic field is plotted as the percentage deviation from the average value in the racetrack core region (between -14.5 mm and 14.5 mm). The feedback magnetic field does not deviate by more than 0.42% along the core axis and the feedback coils consume 29.7 mW to null earth field. (b) The measured percentage deviation of the magnetic field for each position

295   **along the axis of the ring-core hole. The magnetic field deviates as much as 5.62% in the domain of the one-inch ring-core (between -12.7 mm and 12.7 mm).**

3.1.1 Comparison with Ring-core Feedback Field

We performed the same test again, this time using our prototype feedback winding for our 1" ring-core sensor (Figure 1b) which has similar geometry to its heritage e-POP design (Wallis et al., 2016) and many historical missions (e.g. Acuña, 1980). The ring-

300   core sensor uses solenoidal windings which have similar dimensions for all three axes, so we expect the feedback field to be roughly the same for each axis. Figure 9 plots the measured magnetic flux distribution along the radial axis of the ring-core as a percentage deviation from the average field value in this region. Distance is measured from the center of the ring-core and the ring-core itself extends from 12.7 mm to -12.7 mm.

The maximum that the measured feedback field deviates from uniformity along the x axis of the ring-core sensor is 5.62%. The

305   ring-core feedback windings generate a field the along the center axis of the ring-core that is ten times more inhomogeneous than that generated by the Tesseract sensor.

3.1.2 Comparison with Biot-Savart Model

The feedback configuration of Prototype 3 (Figure 7c), with 864 turns of 40 AWG wire on each axis, was chosen to be the current high-fidelity sensor (Figure 1a) and will be flown on future missions. This feedback winding generates a magnetic field along the

310   axis of its cores that deviates from average by a maximum of 0.42% in the x axis, 0.39% in the y axis and 0.26% in the z axis. To assess the effectiveness of our Biot-Savart simulation experimentally, we directly compared these data to the model output for the field values along the axis of the racetrack bore hole. The results of the model are plotted for each axis as solid lines (Figure 8).
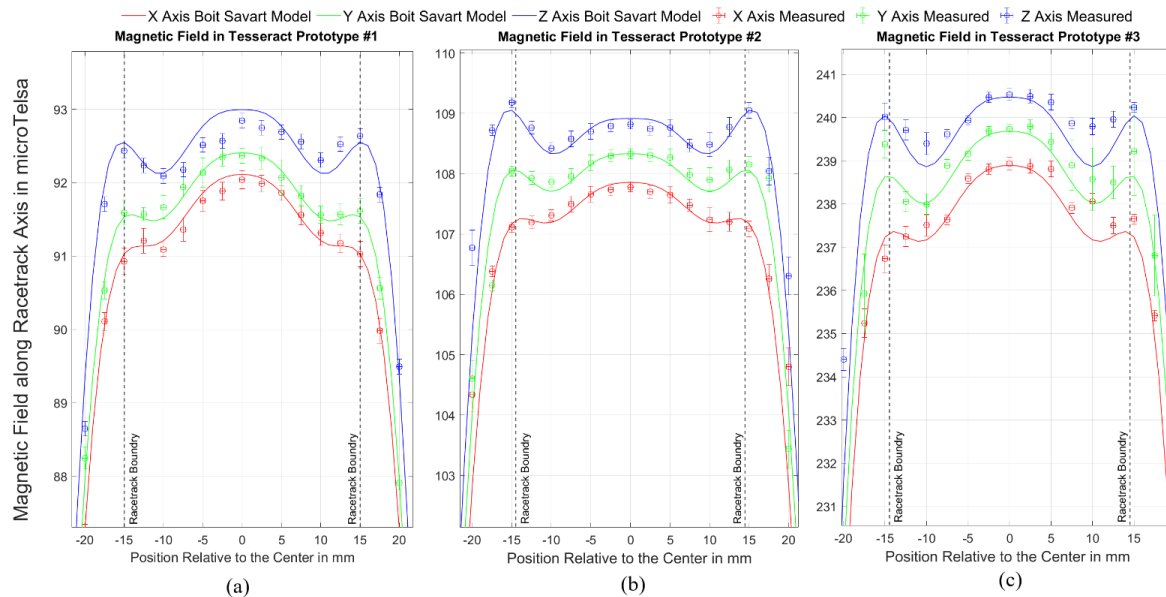
Figure 8: The measured values of the magnetic field for each position along the axis of the racetrack bore hole are plotted as circles with

315   **their corresponding error bars. The output Biot-Savart simulation at the location of the racetrack core is plotted as a solid line.**

Slight differences between the field in the three axes are due to Tesseract's different sized feedback loops that are necessary to nest the physical coils (Figure 1a). The simulation does a reasonable job of modeling the data within the error bars. To quantify the goodness of the model's fit to the data, the square root of the variance of the residuals (RMSE) and the adjusted R-Squared

320   values were calculated for each axis and for each of the three prototypes. The Biot-Savart model fits the data to well above an adjusted R-Squared value of 0.95 and an RMSE below 5.0 for each axis of each prototype sensor. The quality of

these fits implies a very strong agreement between the data and the model, and we take this as an experimental validation of our Biot-Savart simulation.

3.2 Calibration over Temperature

325 One of the main causes of fluxgate instability is the tendency of sensor's intrinsic calibration parameters to change due to thermal variations in the sensor. The fluxgate sensor's sensitivity and orthogonality have long been known to vary with sensor temperature (Trigg et a1 1971). Thus, a characterization of the sensor's calibration parameters over the temperature range that would be expected on magnetospheric, or planetary mission is critical for the validation of a space-based fluxgate sensor.

The dominant effect of changes in temperature on a three-axis null sensor is the change in sensitivity due to variations in the
330 geometry of the coils of wire used to provide magnetic feedback (Primdahl and Jensen, 1982) which is in turn dependent on the rate of thermal expansion or contraction of the material of the bobbin upon which the feedback coils are wound. (Acuña et al., 1978). The temperature dependent sensitivity can be corrected to first order by fluxgate electronics using compensated feedback current (Primdahl, 1970; Acuña et al., 1978; Miles et al., 2017). Another cause of instability is the tendency of the sensor's three orthogonal feedback coils to skew over changes in sensor temperature (Ripka, 1992); however, no equivalent compensation exists
335 for orthogonality so while smaller temperature dependent sensitivity is desirable, smaller orthogonality dependence is more critical.

3.2.1 Experimental Apparatus

Accurately measuring sensitivity and orthogonality over temperature is notoriously challenging, notably due to the difficulty of keeping the excitation/calibration coils thermally isolated from the sensor to ensure that measured changes result from the sensor under test rather than changes in the experimental apparatus. This test usually requires sophisticated equipment. simpler, low-cost
340 methods have been devised (i.e., Brauer et al., 1999; Miles et al., 2017) to calibrate a magnetometer using an insulated cooler filled with dry ice placed within some form of calibration coil.
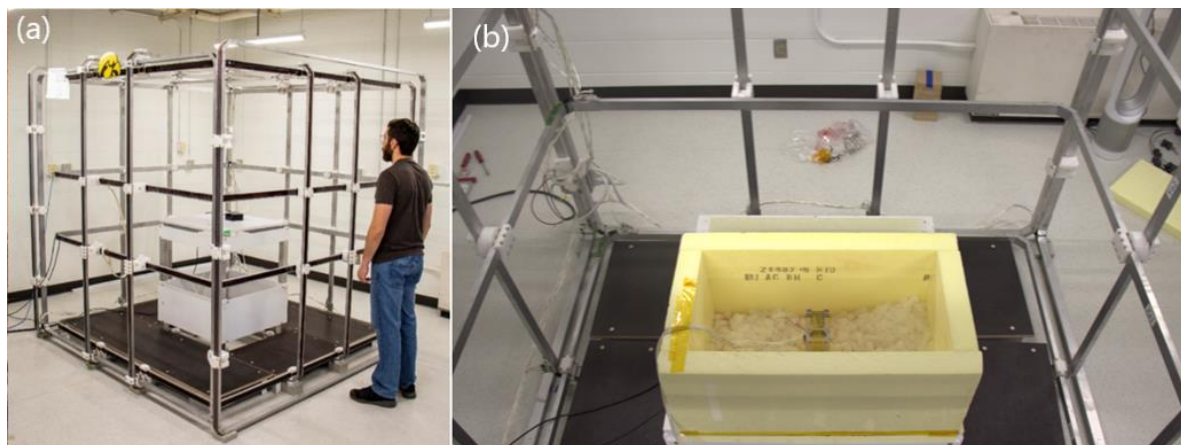
Figure 9: a) The Tesseract prototype is secured in the center of a two-meter Merritt coil system. This coil system is used to generate a field against which the Tesseract can be calibrated. (b) The sensor is secured inside a polystyrene box and the box is filled with dry ice
345 **and a Styrofoam lid is placed on top.**

To characterize the thermal stability of the Tesseract sensor's design, we temporarily configured it as an air-core search coil magnetometer to directly access the attributes of the sensor base and feedback windings without any dependence on cores or electronics. The sensor is placed in a thermally insulated box made from 10 cm thick polystyrene to create a controlled temperature
350 environment for the sensor. The polystyrene box is then placed within the two-meter Merritt coil system and fixed to the table so

that Tesseract's axes are aligned with the coil systems axes as shown in Figure 9a. The coil system was used to generate a 60,000 nT, AC magnetic field at 23 Hz in the x axis for 2 minutes. The same field is then applied on the Y and Z axes, and the coil system is set to cycle through X, Y and Z, so that a complete measurement of sensitivity and orthogonality is taken every 6 minutes. A reference vector magnetometer is placed outside of the box, aligned with the coil system, and wrapped in insulating material to

355 monitor the applied AC field and ensure that the magnitude does not vary.
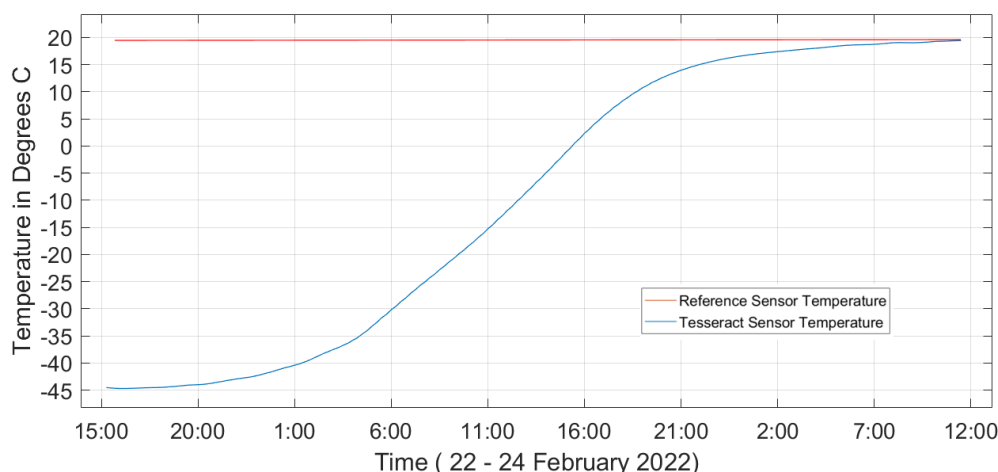
Figure 10: The temperature of the Tesseract sensor (blue) is measured using a platinum RTD as the dry ice sublimates. The temperature of the reference magnetometer (red) was also monitored and found to vary less than 0.1 C over the course of the test.

360 Ten pounds of dry ice is placed inside the box to chill the sensor, and measurements are taken after the dry ice has sublimated and the sensor is slowly warming. A platinum RTD temperature sensor is attached to the sensor and recorded the change in temperature as the sensor returned to room temperature (Figure 10). As the Tesseract sensor temperature slowly increased, the response of the Tesseract prototype sensor's feedback windings, the reference magnetometer and the temperature sensors are digitized and recorded using a common 18-bit National Instruments DAQ.

365 **3.2.2 Feedback Sensitivity and Orthogonality over Temperature**

To evaluate the feedback sensitivity and orthogonality, a finite Fourier transform is performed for each 2-minute segment of data where the 23 Hz field is applied in X then Y then Z. The measured amplitudes of these signals at 23 Hz are recorded for each axis. This yields nine values that define the calibration of the sensor. The sensitivity or gain on each axis is simply the output of the feedback winding when the 60,000 nT field is applied in that direction. Figure 11a plots the measured change in sensitivity

370 measured in the X Y and Z feedback windings in parts per million over changes in temperature. The Tesseract sensor's three orthogonality angles; the angles between the X and Y axes, X and Z axes and Y and Z axes, can be found using simple trigonometry and are defined as:

$$XY = \cos^{-1}\frac{Yy}{A} \tag{2}$$

$$XZ = \sin^{-1}\frac{Zx}{A} \tag{3}$$

375

$$YZ = \sin^{-1}\frac{Zy}{A} \tag{4}$$

Where Yy is the field measured in the Y axis when the coil system applies a field in Y, Zx is the field measured in X when a field is applied in Z, and Zy is the field measured in Y when a field is applied in Z. A is the total magnitude of the applied field. Figure 11b plots each of these angles over temperature.
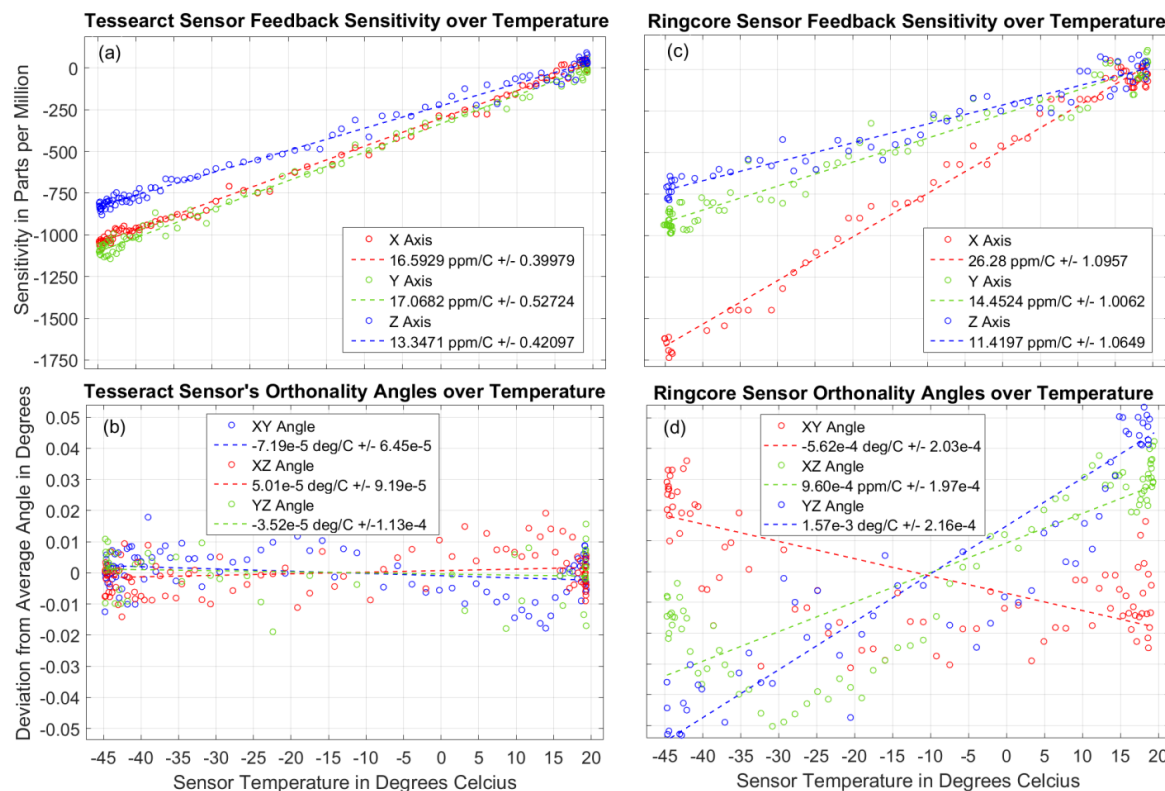
Figure 11: (a) The measured sensitivity of the Tesseract Sensor's three feedback windings plotted against temperature. Each circle is a two-minute measurement of the amplitude of the 60,000nT, 23 Hz signal. The dotted lines are a robust linear fit to the data. The fits estimate that the Tesseracts sensitivity over temperature (b) The Tesseract sensor's three orthogonality angles, XY, XZ and YZ, plotted as a function of sensor temperature. None of the angles are found to unambiguously skew more than 0.015 degrees. (c) The measured sensitivity of the ring-core sensor's three feedback winding plotted against temperature. (d) The ring-core sensors' orthogonality angles are found to skew over temperature by as much as 0.09 degrees

Notwithstanding this modest experimental setup, we are able to measure the sensor's change in sensitivity and orthogonality over temperature. A robust linear fit to the data gives an estimate of the linear dependence of sensitivity on temperature. In all three axes, the sensitivities to temperature are very linear with R squared values of 0.995. We expect that this will make temperature compensation very effective, since the compensation method used by Acuña (1978) is strictly linear. The sensitivity to temperature in the X and Y axes is 16.6 ppm/°C and 17.1 ppm/°C respectively; very comparable to the thermal coefficient of expansion of copper (16.7 ppm/°C) and of the Torlon base material (16.2 ppm/°C) as predicted by Acuña et al., 1978. The Z axis, which is aligned with the direction that Torlon extrusion was injected into the mold during manufacturing, differs slightly (13.3 ppm/°C). Over the course of the test, the signal measured by the reference magnetometer does not vary more than 20 ppm in each axis which confirms that these changes in sensitivity are due to changes in the sensor's feedback windings and not the applied field.

We do not measure any variation in axis alignment to within deviations of 0.015 degrees over changes in temperature from -45°C to 20°C. The sensor's feedback windings are a less-than-ideal search coil, so the accuracy of the measurements is limited by poor

signal. The background magnetic noise of the laboratory also limits the accuracy of this test. This test will be repeated once the
400 sensor is integrated into a functioning fluxgate instrument in a magnetically quite facility in order to verify its flight calibrations.

3.2.4 Comparison with the Ring-core Sensor

The sensitivity and orthogonality of the ring-core's feedback windings over temperature were measured with the same method
described above. The ring-core design sensor (Figure 1b) was also temporarily configured as an air-core search coil magnetometer
so that attributes of the sensor base and feedback windings could be directly measured. The measured sensitivity and orthogonality
405 over temperature are plotted in Figure 11b and Figure 11d.

While the Tesseract and ring-core sensors have comparable thermal sensitivities, the Tesseract's sensitivity over temperature is
more consistent in each axis, presumably due to the greater symmetry of the sensor's feedback windings. The ring-core sensors'
orthogonality angles skew by as much as 0.09 degrees (Figure 11d). The YZ Angle (blue) changes the most, presumably because
the ring-core sensor base is most asymmetric between the Y and Z Axes (Figure 1b).

410 3.3 Sensor Noise

The noise floor of a fluxgate is typically limited by the intrinsic magnetic noise of a ferromagnetic core that is periodically driven
into magnetic saturation to modulate the local magnetic field. The noise floor on Tesseract's custom miniature racetrack cores was
characterized in Miles (2022). A single-axis electronics board was used to drive and sample each fluxgate core. The power spectral
density noise floor of the instrument was estimated by using 20 minutes of data while the racetrack sensors were inside a single
415 axis four-layer mumetal magnetic shield. The noise floor for the racetrack core sensors that will be used in Tesseract were
determined to be 5 pT/√Hz at 1Hz (Miles et al., 2022).

4 Conclusions

The novel fluxgate sensor called Tesseract has been designed and prototyped. It is a low mass, low noise sensor that mitigates
420 several known causes of instability in the 1" ring-core design. We modeled the sensor's feedback winding using a Biot-Savart
simulation and used it to optimize the Tesseract Sensor's feedback topology for homogeneity and power consumption. The
simulation results were in agreement with laboratory measurements of the prototype sensors' feedback magnetic field. The
Tesseract retains its ferromagnetic cores in a feedback magnetic field that homogeneous to within deviations of 0.42%

We used a low-cost method to analyze the sensor's gain and orthogonality over temperature. This method uses coil system
425 measurements and a second reference magnetometer to least squares vector-vector calibration to find the intrinsic sensitivity,
orthogonality, and offsets of the sensor as a function of temperature. Using this method, we show that the Tesseract's three
orthogonal axes skew by no more than 0.015 degrees over changes in temperature from -45 °C to 20 °C. The Tesseract sensor
outperforms the traditional 1" ring-core Sensor design in both these metrics. The Tesseract's orthogonal axes are more stable by
at least a factor of 4 and its magnetic feedback is more homogenous by a factor of 13. We surmise that Tesseract's higher degree
430 of feedback homogeneity and axis stability over temperature will contribute to improved fluxgate stability.

4.1 Future Work

The accuracy of these measurements is limited by the magnetic noise of the laboratory setup. A more sophisticated experimental
set up will be required to characterize the stability of Tesseract's calibration parameters to an accuracy acceptable for most space
435 science applications (greater than ± 0.1 nT). We are currently developing a new calibration facility at the University of Iowa
calibration facility that will be purpose built for characterizing fluxgate sensor's calibration parameters over temperature. In future

studies, we hope to use the specialized, environmentally controlled Helmholtz coil facility at Goddard Space Flight Center that would be capable of resolving Tesseract's long-term stability to a precision of ± 200 pT. (Vernier et al., 2004). Fluxgate electronics are currently being developed for the Tesseract Sensor in preparation for upcoming flights. Once the sensor has been integrated

440   with cores and electronics, the Tesseract will be characterized again as a complete flight-ready fluxgate instrument. Tesseract will be flight demonstrated on the ACES-II sounding rockets, currently scheduled to launch in December 2022 and again aboard the TRACERS satellite mission as part of the MAGIC technology demonstration which is scheduled to launch in 2023.

Code and Data Availability

445   Data and source code used in the creation of this paper can be accessed by contacting the authors.

Author Contributions

K. Greene led the design, assembly, and execution of the experiments, analysed the data, created the feedback field simulation and wrote the manuscript with contributions from all authors. D. M. Miles provided supervision and funding of the project as the lead

450   investigator and assisted in the interpretation of the data. C. Hansen led the development and manufacture of the Tesseract Sensor prototypes. B. B. Narod conceptualized the Tesseract sensor design. R. Dvorsky assisted with the design of the sensor prototypes and testing apparatus.

Competing Interests

455   B. B. Narod operated Narod Geophysics Ltd., which manufactured fluxgate magnetometers until the company ceased production operation in 2008.

Acknowledgments

The authors are greatly indebted to Suman Sherwani and Amanda Lasko. This work would not have been possible if it were not for their oversight and management of the prototype manufacturing and testing processes. Special thanks to Samuel Hisel, Antonio

460   Washington and Alex Hoffman for lending their expertise to laboratory electronics and software, and for their flexibility in managing hardware that made this experimental work feasible. Special thanks to Michael D Webb lending his expertise to laboratory equipment. The authors would also like to thank Steve Klinkhammer and Ryan Helland for their manufacturing efforts and Katherine Deasy for her work in configuration management.

465   Early development activities and much of the research infrastructure used in this work was supported by faculty start-up funding for David Miles from the University of Iowa. This material is based upon work supported by the National Aeronautics and Space Administration under Grant No. 80NSSC19K0491 issued through the Science Mission Directorate and Contract No. 80GSFC18C0008 administered by Goddard Space Flight Center

470 **References**

Acuña, M. H. and Ness, N. F.: The Magnetic Field of Saturn: Pioneer 11 Observations, Science, 207, 444–446, https://doi.org/10.1126/science.207.4429.444, 1980.

Acuña, M. H., Scearce, C. S., Seek, J., and Scheifele, J.: The MAGSAT vector magnetometer: A precision fluxgate magnetometer
475 for the measurement of the geomagnetic field, 1978.

Auster, H. U., Glassmeier, K. H., Magnes, W., Aydogar, O., Baumjohann, W., Constantinescu, D., Fischer, D., Fornacon, K. H., Georgescu, E., Harvey, P., Hillenmaier, O., Kroth, R., Ludlam, M., Narita, Y., Nakamura, R., Okrafka, K., Plaschke, F., Richter, I., Schwarzl, H., Stoll, B., Valavanoglou, A., and Wiedemann, M.: The THEMIS Fluxgate Magnetometer, Space Sci Rev, 141,
480 235–264, https://doi.org/10.1007/s11214-008-9365-9, 2008.

Balogh, A., Carr, C. M., Acuña, M. H., Dunlop, M. W., Beek, T. J., Brown, P., Fornacon, K.-H., Georgescu, E., Glassmeier, K.-H., Harris, J., Musmann, G., Oddy, T., and Schwingenschuh, K.: The Cluster Magnetic Field Investigation: overview of in-flight performance and initial results, Ann. Geophys., 19, 1207–1217, https://doi.org/10.5194/angeo-19-1207-2001, 2001.
485

Bandyopadhyay, S., Subramanian, G. P., Foust, R., Morgan, D., Chung, S.-J., and Hadaegh, F.: A Review of Impending Small Satellite Formation Flying Missions, in: 53rd AIAA Aerospace Sciences Meeting, 53rd AIAA Aerospace Sciences Meeting, Kissimmee, Florida, https://doi.org/10.2514/6.2015-1623, 2015.

490 Brauer, P., Merayo, J. M. G., Risbo, T., and Primdahl, F.: Magnetic calibration of vector magnetometers, 10, n.d.
Forslund, Å., Belyayev, S., Ivchenko, N., Olsson, G., Edberg, T., and Marusenkov, A.: Miniaturized digital fluxgate magnetometer for small spacecraft applications, Meas. Sci. Technol., 19, 015202, https://doi.org/10.1088/0957-0233/19/1/015202, 2008.

Ganushkina, N., Jaynes, A., and Liemohn, M.: Space Weather Effects Produced by the Ring Current Particles, Space Sci Rev, 212,
495 1315–1344, https://doi.org/10.1007/s11214-017-0412-2, 2017.

Garrick-Bethell, I., Paige, D. A., Burton, M., Boland, J., Abrahams, J. N. H., Bogert, C. van der, Choi, Y.-J., Deca, J., Hanna, K. D., Farrell, W. M., Hemingway, D., Hiesinger, H., Jin, H., Johnson, B. C., Kaluna, H., Kelley, M. R., Larson, D. E., Lawrence, D. J., Li, S., Ma, Y., Maxwell, R. E., Miller, R. S., Pieters, C. M., Poppe, A. R., Ravat, D., Russell, C. T., Siegler, M. A., Vernazza,
500 P., and Weiss, B. P.: NanoSWARM: NanoSatellites for Space Weathering, Surface Water, Solar Wind, and Remanent Magnetism, 53, https://doi.org/10.3847/25c2cfeb.314447c9, 2021.

Grosz, A., Haji-Sheikh, M. J., and Mukhopadhyay, S. C. (Eds.): High Sensitivity Magnetometers, Springer International Publishing, Cham, https://doi.org/10.1007/978-3-319-34070-8, 2017.
505

Kepko, L., Clagett, C., Santos, L., Azimi, B., Berry, D., Bonalsky, T., Chai, D., Cudmore, A., Evans, A., Hesh, S., Jones, S., Marshall, J., Paschalidis, N., Rodriquez, J., Rodriquez, M., Sheikh, S., Starin, S., and Zesta, E.: Dellingr: NASA Goddard Space Flight Center's First 6U Spacecraft, 12, 2017.

510 Magdaleno-Adame, S., Olivares-Galvan, J. C., Campero-Littlewood, E., Escarela-Perez, R., Blanco-Brisset, E..: COSMOL Conference, Boston, USA, July 5 Coil Systems to Generate Uniform Magnetic Field Volumes, 7, 2010.

Maruca, B. A., Agudelo Rueda, J. A., Bandyopadhyay, R., Bianco, F. B., Chasapis, A., Chhiber, R., DeWeese, H., Matthaeus, W. H., Miles, D. M., Qudsi, R. A., Richardson, M. J., Servidio, S., Shay, M. A., Sundkvist, D., Verscharen, D., Vines, S. K., Westlake,
515 J. H., and Wicks, R. T.: MagneToRE: Mapping the 3-D Magnetic Structure of the Solar Wind Using a Large Constellation of Nanosatellites, Front. Astron. Space Sci., 8, 665885, https://doi.org/10.3389/fspas.2021.665885, 2021
.
Merayo, JMG, Jørgensen JL, Friis-Christensen E, Brauer P, Primdahl F, Jørgensen PS, Allin TH, Denver T. The Swarm magnetometry package. InSmall satellites for Earth observation (pp. 143-151). Springer, Dordrecht. 2008.
520
Merritt, R., Purcell, C., and Stroink, G.: Uniform magnetic field produced by three, four, and five square coils, Review of Scientific Instruments, 54, 879–882, https://doi.org/10.1063/1.1137480, 1983.

Miles, D. M., Mann, I. R., Ciurzynski, M., Barona, D., Narod, B. B., Bennest, J. R., Pakhotin, I. P., Kale, A., Bruner, B., Nokes,
525 C. D. A., Cupido, C., Haluza-DeLay, T., Elliott, D. G., and Milling, D. K.: A miniature, low-power scientific fluxgate magnetometer: A stepping-stone to cube-satellite constellation missions: A Miniature Fluxgate Magnetometer, J. Geophys. Res. Space Physics, 121, 11,839-11,860, https://doi.org/10.1002/2016JA023147, 2016.

Miles, D. M., Mann, I. R., Kale, A., Milling, D. K., Narod, B. B., Bennest, J. R., Barona, D., and Unsworth, M. J.: The effect of
530 winding and core support material on the thermal gain dependence of a fluxgate magnetometer sensor, Geosci. Instrum. Method. Data Syst., 6, 377–396, https://doi.org/10.5194/gi-6-377-2017, 2017.

Miles, D. M., Ciurzynski, M., Barona, D., Narod, B. B., Bennest, J. R., Kale, A., Lessard, M., Milling, D. K., Larson, J., and Mann, I. R.: Low-noise permalloy ring cores for fluxgate magnetometers, Geosci. Instrum. Method. Data Syst., 8, 227–240,
535 https://doi.org/10.5194/gi-8-227-2019, 2019.

Miles, D. M., Dvorsky, R., Greene, K., Hansen, C. T., Narod, B. B., and Webb, M. D.: Contributors to fluxgate magnetic noise in permalloy foils including a potential new copper alloy regime, Geosci. Instrum. Method. Data Syst., 11, 111–126, https://doi.org/10.5194/gi-11-111-2022, 2022.
540
Moldovanu, A., Chiriac, H., Moldovanu, C., Macoviciuc, M., and Ioan, C.: Performances of the fluxgate sensor with tensile stress annealed ribbons, Sensors and Actuators A: Physical, 81, 189–192, https://doi.org/10.1016/S0924-4247(99)00085-0, 2000.

Nakariakov, V. M., Pilipenko, V., Heilig, B., Jelínek, P., Karlický, M., Klimushkin, D. Y., Kolotkov, D. Y., Lee, D.-H., Nisticò,
545 G., Van Doorsselaere, T., Verth, G., and Zimovets, I. V.: Magnetohydrodynamic Oscillations in the Solar Corona and Earth's

Magnetosphere: Towards Consolidated Understanding, Space Sci Rev, 200, 75–203, https://doi.org/10.1007/s11214-015-0233-0, 2016.

Narod, B. B. and Bennest, J. R.: Ring-core fluxgate magnetometers for use as observatory variometers, Physics of the Earth and
550   Planetary Interiors, 59, 23–28, https://doi.org/10.1016/0031-9201(90)90205-C, 1990.

Pfaff, R. F., Jr.: An Overview of the Scientific and Space Weather Motivation for the Notional Geospace Dynamics Constellation Mission, AGU Fall Conference, San Francisco, CA, December 13, SA23C-01, 2016.

555   Primdahl, F.: Temperature compensation of fluxgate magnetometers, IEEE Trans. Magn., 6, 819–822, https://doi.org/10.1109/TMAG.1970.1066971, 1970.

Primdahl, F.: The fluxgate magnetometer, J. Phys. E: Sci. Instrum., 12, 241–253, https://doi.org/10.1088/0022-3735/12/4/001, 1979.

560

Primdahl, F. and Jensen, P. A.: Compact spherical coil for fluxgate magnetometer vector feedback, J. Phys. E: Sci. Instrum., 15, 221–226, https://doi.org/10.1088/0022-3735/15/2/015, 1982.

Ripka, P.: Review of fluxgate sensors, Sensors and Actuators A: Physical, 33, 129–141, https://doi.org/10.1016/0924-
565   4247(92)80159-Z, 1992.

Ripka, P.: Advances in fluxgate sensors, Sensors and Actuators A: Physical, 106, 8–14, https://doi.org/10.1016/S0924-4247(03)00094-3, 2003.

570   Slavin, J. A., Le, G., Strangeway, R. J., Wang, Y., Boardsen, S. A., Moldwin, M. B., and Spence, H. E.: Space Technology 5 multi-point measurements of near-Earth magnetic fields: Initial results, Geophys. Res. Lett., 35, L02107, https://doi.org/10.1029/2007GL031728, 2008.

Torbert, R. B., Russell, C. T., Magnes, W., Ergun, R. E., Lindqvist, P.-A., LeContel, O., Vaith, H., Macri, J., Myers, S., Rau, D.,
575   Needell, J., King, B., Granoff, M., Chutter, M., Dors, I., Olsson, G., Khotyaintsev, Y. V., Eriksson, A., Kletzing, C. A., Bounds, S., Anderson, B., Baumjohann, W., Steller, M., Bromund, K., Le, G., Nakamura, R., Strangeway, R. J., Leinweber, H. K., Tucker, S., Westfall, J., Fischer, D., Plaschke, F., Porter, J., and Lappalainen, K.: The FIELDS Instrument Suite on MMS: Scientific Objectives, Measurements, and Data Products, Space Sci Rev, 199, 105–135, https://doi.org/10.1007/s11214-014-0109-8, 2016.

580   Wallis, D. D., Miles, D. M., Narod, B. B., Bennest, J. R., Murphy, K. R., Mann, I. R., and Yau, A. W.: The CASSIOPE/e-POP Magnetic Field Instrument (MGF), Space Sci Rev, 189, 27–39, https://doi.org/10.1007/s11214-014-0105-z, 2015.